European Journal of Mechanics / A Solids 121 (2027) 106311

Contents lists available at ScienceDirect

European Journal of Mechanics / A Solids

journal homepage: www.elsevier.com/locate/ejmsol

Full length article

Unveiling synergetic enhancement of strength and ductility in nanovoid-strengthened metals

Quanfeng Han [a,b], Jiaji Chen [c], Yufei Gao [d], Wenlong Li [e], Huiru Guo [a,b], Hui Wang [a,b], Yizhe Chen [a,b,*], Xin Yi [f,*], Lin Hua [a,b,*]

[a] State Key Laboratory of Light Superalloys, Wuhan University of Technology, Wuhan 430070, China
[b] School of Automotive Engineering, Wuhan University of Technology, Wuhan 430070, China
[c] Interdisciplinary Research Center, Liaoning Academy of Materials, Shenyang 110000, China
[d] China Nuclear Power Technology Research Institute Co., Ltd., Shenzhen 518038, China
[e] National Key Laboratory of Aerospace Liquid Propulsion, Xi'an Aerospace Propulsion Institute, Xi'an 710100, China
[f] School of Mechanics and Engineering Science, Peking University, Beijing 100871, China

ARTICLE INFO

Keywords:
Porous metallic materials
Dislocation–nanovoid interaction
Strengthening mechanisms
Strength–ductility synergy
Constitutive modeling

ABSTRACT

Voids degrade the strength of metallic materials and accelerate fracture. However, our experiments have demonstrated a breakdown of the strength–ductility trade-off in gold by introducing dispersed nanovoids. Till now, the underlying strengthening mechanism remains unclear, as the previously proposed Orowan-based interpretation contradicts the observed dislocation–nanovoid cutting behavior in experiments and molecular dynamics simulations. In this research, a physics-based constitutive model that incorporates competition among different dislocation–nanovoid interaction mechanisms was developed to reveal the dominant strengthening mechanism. The yield strength and ductility predicted by the proposed constitutive model agree well with the experimental results for both dense gold and porous gold with dispersed nanovoids. It is shown that the weak-cutting mechanism, involving the formation of new matrix surfaces, governs the strength enhancement across a wide range of void sizes, rather than the Orowan mechanism previously assumed. Moreover, the increased ductility arises from strengthening induced by nanovoid growth and from nanovoid-enhanced dislocation accumulation. Based on these findings, an efficient prediction model for yield strength and a quantitative criterion for maintaining ductility were developed to conveniently assess macroscopic mechanical performance. This study provides mechanistic insight and practical guidance for designing nanovoid-engineered metallic materials with optimized strength and ductility.

1. Introduction

Metallic materials that combine low density with a favorable strength–ductility balance are highly desirable for engineering structures, as they can improve energy efficiency and reduce carbon footprint. In addition to alloying with lightweight elements such as aluminum, magnesium, and lithium, an alternative strategy is to tailor the material' s hierarchical architecture at multiple length scales (Chen et al., 2025; Kim et al., 2025; Chen et al., 2026; Dai et al., 2026). At the macroscopic scale, metallic lattices incorporating triply periodic minimal surfaces or multi-phase architectures exhibit superior energy absorption and high specific stiffness and strength under compressive loading (Pham et al., 2019; Huang et al., 2025). At the mesoscale, reducing the mean domain size to the micrometer level enhances tensile ductility in porous Fe–Mn–Cr alloys prepared by dealloying, primarily due to the introduction of a high density of weak boundaries (Xie et al., 2023). At the nanoscale, the presence of nanovoids — such as helium bubbles — can impede dislocation motion and significantly strengthen metallic materials (Hu et al., 2016; Ji et al., 2023). However, this strengthening is often accompanied by reduced ductility owing to helium-induced embrittlement, resulting in a pronounced strength–ductility trade-off (Hure et al., 2022; Changizian et al., 2023). The dual role of pores and voids thus presents both opportunities and challenges for achieving strength–ductility synergy in porous metallic materials.

In general, large pores and voids degrade the strength of metallic materials and accelerate fracture under tensile loading. However, our recent experimental study has reported an unexpected nanovoid-enhanced strength–ductility synergy in gold, achieved without altering the materials composition or phase (Chen et al., 2024). As the average

* Corresponding authors.
E-mail addresses: yzchen@whut.edu.cn (Y. Chen), xyi@pku.edu.cn (X. Yi), hualin@whut.edu.cn (L. Hua).

https://doi.org/10.1016/j.euromechsol.2026.106311
Received 15 June 2026; Received in revised form 20 July 2026; Accepted 22 July 2026
Available online 27 July 2026

nanovoid diameter decreased from 180 to 18 nm, the experimentally measured yield strength of the porous gold increased from 116 to 176 MPa, around 36% and 107% larger than that of dense gold, respectively. In addition, compared with the original tensile elongation 11.5% of dense gold, the maximum relative increase in tensile elongation exceeds 45% for the porous gold. Assuming that nanovoids act as impenetrable obstacles to dislocation motion, we previously attributed the strengthening effect to the Orowan bypassing mechanism and developed a quantitative model that explains the experimentally observed evolution of yield strength. This unconventional observation offers new insights into designing lightweight metallic materials with superior synergistic mechanical performance. Nevertheless, the physical origin of the yield strength enhancement induced by nanovoids remains not fully understood.

Numerous experimental studies have demonstrated that the interaction between dislocations and precipitates in metallic materials is strongly size-dependent (Li et al., 2024; Yuan et al., 2025). As the characteristic precipitate size decreases from hundreds of nanometers to several nanometers, the governing deformation mechanism transitions sequentially from the Orowan bypassing mechanism to the strong-cutting mechanism and finally to the weak-cutting mechanism (Roger, 2006; Fang et al., 2019). For the nanovoids present in porous gold, a similar size dependence can be expected: at sufficiently small void sizes, dislocations tend to shear through the voids rather than bypass them, since the voids possess lower stiffness and weaker resistance to dislocation motion compared with precipitates. This behavior has been confirmed by both molecular dynamics simulations and experimental observations in metallic systems containing nanovoids with various internal pressures (Ding et al., 2016a,b; Ji et al., 2023; Liu and Demkowicz, 2023; Lin et al., 2026), contrasting with the assumption of impenetrable obstacles. Therefore, it is not rigorous to attribute the strengthening effect of nanovoids solely to the Orowan mechanism. In addition, the observed improvement in ductility is cursorily ascribed to the suppression of low-energy dislocation cell formation by dislocation–void interactions (Chen et al., 2024). However, as nanovoids evolve in both size and volume fraction during deformation, their influence on dislocation slip resistance — and thus on the overall strain hardening and ductility — can vary significantly, irrespective of whether the governing mechanism is cutting or bypassing. Therefore, the physical origin of ductility enhancement in porous metallic materials containing dispersed nanovoids remains unresolved.

To elucidate the fundamental mechanism underlying the enhanced strength–ductility synergy in porous metallic materials containing dispersed nanovoids, this study develops a physics-based crystal plasticity model that explicitly accounts for the competition between the Orowan bypassing and cutting mechanisms. After validating the intrinsic material parameters using the mechanical response of dense gold, a series of numerical simulations is conducted to investigate the nanovoid-regulated deformation and failure behaviors of porous gold. The simulations reveal that the weak-cutting mechanism, associated with the formation of new matrix surfaces, predominates in strengthening across a wide range of void sizes, in contrast to existing theoretical explanations based on the impenetrable obstacle and Orowan mechanism. Furthermore, a theoretical model for predicting yield strength and a quantitative criterion for ensuring ductility are proposed for the first time, providing efficient guidelines for optimizing the strength–ductility balance in nanovoid-engineered metallic materials.

2. Crystal plasticity constitutive model for porous metallic materials with dispersed nanovoids

2.1. General constitutive framework

For metallic materials containing voids with non-zero internal pressure, Yu et al. (2020) proposed a modified Gurson–Tvergaard–Needleman yield potential that captures the coupling among applied stress, void volume fraction, internal pressure, and effective stress

$$\begin{aligned}\Psi =&\left(\frac{\tau_i}{\tau_i^{\mathrm{eff}}}\right)^2+\frac{2f_{\mathrm{v}}^{\mathrm{eff}}P\left|\tau_i\right|}{\left(\tau_i^{\mathrm{eff}}\right)^2}+\frac{2}{45}\lambda f_{\mathrm{v}}^{\mathrm{eff}}\left(\frac{\sigma_{\mathrm{eq}}}{\tau_i^{\mathrm{eff}}}\right)^2\\&+2q_1f_{\mathrm{v}}^{\mathrm{eff}}\cosh\left[q_2\sqrt{\frac{3}{10}\frac{P\sigma_{\mathrm{m}}}{\left(\tau_i^{\mathrm{eff}}\right)^2}+\frac{3}{20}\frac{\sigma_{\mathrm{m}}^2}{\left(\tau_i^{\mathrm{eff}}\right)^2}}\right],\\&-\left(q_1f_{\mathrm{v}}^{\mathrm{eff}}\right)^2-1=0\end{aligned}\tag{1}$$

where the resolved shear stress τ_i acting on the ith slip system is defined by $\tau_i=\boldsymbol{\sigma}:\mathbf{N}_i$, and $\boldsymbol{\sigma}$ is the applied Cauchy stress tensor. The Schmid tensor $\mathbf{N}_i=\mathbf{m}_i\otimes\mathbf{n}_i$ acts as a projection operator that converts the macroscopic stress into the resolved shear stress acting on the ith slip system, where unit vectors $\mathbf{m}_i$ and $\mathbf{n}_i$ are the slip direction and normal of the ith slip system, respectively. Both the von Mises stress σ_{eq} and hydrostatic stress σ_{m} are associated with $\boldsymbol{\sigma}$. Dimensionless parameters q_1, q_2, and λ are variable constants. P denotes the internal pressure of the gas trapped inside the voids. The effective void volume fraction $f_{\mathrm{v}}^{\mathrm{eff}}$ equals to the void volume fraction f_{v} when $f_{\mathrm{v}}\le 1/q_1$, and equals to $1/q_1$ when $f_{\mathrm{v}}>1/q_1$. The effective resolved shear stress τ_i^{eff} is determined by solving Eq. (1) after giving the aforementioned parameters and variables. At $P=0$ MPa, Eq. (1) degrades to the potential function for metallic materials containing voids without internal gas pressure.

The plastic strain rate tensor $\mathbf{D}_{\mathrm{p}}$ of porous metallic materials is defined as (Han et al., 2013)

$$\mathbf{D}_{\mathrm{p}}=\frac{1-f_{\mathrm{v}}}{2}\sum_{i=1}^{N_{\mathrm{s}}}\dot{\gamma}_i[\mathbf{N}_i^{\mathrm{eff}}+(\mathbf{N}_i^{\mathrm{eff}})^{\mathrm{T}}],\tag{2}$$

where $N_{\mathrm{s}}=12$ is the total number of slip systems for the face-centered cubic (FCC) metals at ambient temperature, and $\dot{\gamma}_i$ is the plastic shear rate on the ith slip system, with a dot over it denoting a derivative with respect to time. Using Eq. (1), the normality rule, and the implicit function theorem, the effective Schmid tensor is defined as

$$\mathbf{N}_i^{\mathrm{eff}}=\frac{\partial\tau_i^{\mathrm{eff}}}{\partial\boldsymbol{\sigma}}=-\frac{\partial\Psi/\partial\boldsymbol{\sigma}}{\partial\Psi/\partial\tau_i^{\mathrm{eff}}},\tag{3}$$

where

$$\begin{aligned}\frac{\partial\Psi}{\partial\boldsymbol{\sigma}}=&\frac{2\tau_i}{\left(\tau_i^{\mathrm{eff}}\right)^2}\mathbf{N}_i+\frac{2f_{\mathrm{v}}^{\mathrm{eff}}P\mathrm{sgn}(\tau_i)}{\left(\tau_i^{\mathrm{eff}}\right)^2}\mathbf{N}_i+\frac{2}{15}\frac{\lambda f_{\mathrm{v}}^{\mathrm{eff}}}{\left(\tau_i^{\mathrm{eff}}\right)^2}\mathbf{S}\\&+\frac{q_1q_2f_{\mathrm{v}}^{\mathrm{eff}}}{10\sqrt{\frac{3}{10}\frac{P\sigma_{\mathrm{m}}}{\left(\tau_i^{\mathrm{eff}}\right)^2}+\frac{3}{20}\frac{(\sigma_{\mathrm{m}})^2}{\left(\tau_i^{\mathrm{eff}}\right)^2}}}\\&\times\sinh\left[q_2\sqrt{\frac{3}{10}\frac{P\sigma_{\mathrm{m}}}{\left(\tau_i^{\mathrm{eff}}\right)^2}+\frac{3}{20}\frac{(\sigma_{\mathrm{m}})^2}{\left(\tau_i^{\mathrm{eff}}\right)^2}}\right]\times\frac{P+\sigma_{\mathrm{m}}}{\left(\tau_i^{\mathrm{eff}}\right)^2}\mathbf{I}\end{aligned}\tag{4}$$

and

$$\begin{aligned}\frac{\partial\Psi}{\partial\tau_i^{\mathrm{eff}}}=&-\frac{2\tau_i^2}{\left(\tau_i^{\mathrm{eff}}\right)^3}-\frac{4f_{\mathrm{v}}^{\mathrm{eff}}P\left|\tau_i\right|}{\left(\tau_i^{\mathrm{eff}}\right)^3}-\frac{4}{45}\frac{\lambda f_{\mathrm{v}}^{\mathrm{eff}}\sigma_{\mathrm{eq}}^2}{\left(\tau_i^{\mathrm{eff}}\right)^3}\\&-\frac{2q_1q_2f_{\mathrm{v}}^{\mathrm{eff}}}{\tau_i^{\mathrm{eff}}}\sqrt{\frac{3}{10}\frac{P\sigma_{\mathrm{m}}}{\left(\tau_i^{\mathrm{eff}}\right)^2}+\frac{3}{20}\frac{\sigma_{\mathrm{m}}^2}{\left(\tau_i^{\mathrm{eff}}\right)^2}}\\&\times\sinh\left[q_2\sqrt{\frac{3}{10}\frac{P\sigma_{\mathrm{m}}}{\left(\tau_i^{\mathrm{eff}}\right)^2}+\frac{3}{20}\frac{\sigma_{\mathrm{m}}^2}{\left(\tau_i^{\mathrm{eff}}\right)^2}}\right]\end{aligned}\tag{5}$$

with the deviatoric stress tensor $\mathbf{S}=\boldsymbol{\sigma}-\sigma_{\mathrm{m}}\mathbf{I}$ and second-order identity tensor $\mathbf{I}$.

The plastic shear rate $\dot{\gamma}_i$ is described phenomenologically as (Hutchinson, 1976)

$$\dot{\gamma}_i=\dot{\gamma}^0\left|\frac{\tau_i^{\mathrm{eff}}}{\tau_i^{\mathrm{c}}}\right|^{1/m}\mathrm{sgn}(\tau_i^{\mathrm{eff}}),\tag{6}$$

where $\dot{\gamma}^0$ is the reference shear strain rate, m is the dimensionless rate-sensitivity exponent, and τ_i^c denotes the critical resolved shear stress (CRSS) of the ith slip system. The parameter m ranges from the order of 10^{-3} to 10^{-2} for the low viscous metallic materials at ambient temperature.

For the porous metallic materials with dispersed nanovoids, both dislocation interactions and nanovoid–dislocation interactions contribute to the flow resistance. Since lattice friction is negligible in FCC metals, the CRSS is expressed as

$$\tau_i^c = \tau_i^d + \tau_i^v, \tag{7}$$

where $\tau_i^d = \alpha\mu b\sqrt{\rho_i}$ represents the dislocation hardening contribution, with α the dislocation hardening coefficient reflecting the contribution of microscopic dislocations to the macroscopic yield behavior, μ the shear modulus, b the Burgers vector magnitude, and ρ_i the dislocation density belonging to the ith slip system. The term τ_i^v accounts for the strengthening induced by nanovoids, which will be modeled and discussed in detail in the following section. The evolution rate of dislocation density $\dot{\rho}_i$ follows (Li et al., 2025)

$$\dot{\rho}_i = \frac{1}{b}\left(\frac{\sqrt{\rho_i}}{K} - 2y_c\rho_i\right)|\dot{\gamma}_i|, \tag{8}$$

where K is a dimensionless material parameter governing the dislocation accumulation, and y_c is the critical annihilation distance between dislocations. Small K and y_c result in rapid accumulation and slow annihilation of intragranular dislocation, respectively, mathematically increasing the strain hardening ability of materials.

2.2. Strengthening mechanism driven by nanovoids

The interaction mechanism between dislocations and obstacles, such as precipitates or voids, depends on the obstacle size (Roger, 2006; Fang et al., 2019). For relatively large precipitates, dislocations bypass these precipitates by bowing between them, forming semicircular loops. The corresponding increase in slip resistance is classically described by the Orowan relation (Orowan, 1948)

$$\tau_{\text{Orowan}} = \frac{2T^d}{bL}, \tag{9}$$

where T_d is the dislocation line tension, $L = d_v(\sqrt{\pi/6f_v} - 1)$ is the mean planar spacing between adjacent precipitates with d_v as the obstacle diameter. Considering the softening effect due to the self-interaction among adjacent bowing dislocation loops, modified Orowan formulas have been proposed by introducing the harmonic mean of the precipitate spacing and diameter (Bacon et al., 1973; Osetsky et al., 2003). However, the prediction accuracy of this approach, also adopted in our previous work (Chen et al., 2024), relies on experimentally measured yield strengths, as the fitted dimensionless parameters lack physical meaning.

As precipitate size decreases, a dislocation can cut through the precipitate, forming an anti-phase boundary (APB) and a new matrix–particle interface. Creating new interfaces in materials increases slip resistance to dislocation motion. For relatively large precipitates, the dislocation–precipitate interaction occurs via the strong-cutting mechanism, and the additional shear stress required for cutting obstacles is (Reppich, 1975)

$$\tau_{\text{strong}} = \frac{1}{2}\left(\frac{\gamma_{\text{APB}}}{b} + \frac{2\gamma_{\text{surf}}}{d_1}\right)\frac{d_1}{L} - \frac{1}{2}\left(\frac{\gamma_{\text{APB}}}{b} - \frac{2\gamma_{\text{surf}}}{d_2}\right)f_v, \tag{10}$$

where d_1 and d_2 are the line lengths of edge dislocations within the pair-coupled precipitates, both on the order of the precipitate diameter. γ_{APB} and γ_{surf} denote the APB energy and surface energy, respectively. At sufficiently small precipitate sizes, the weak-cutting mechanism dominates, and the corresponding increase in CRSS is given by (Reppich, 1975)

$$\tau_{\text{weak}} = \frac{1}{2}\sqrt{\left(\frac{\gamma_{\text{APB}}}{b} + \frac{2\gamma_{\text{surf}}}{d_1}\right)^3\frac{bd_1^3}{2T^dL^2}} - \frac{1}{2}\left(\frac{\gamma_{\text{APB}}}{b} - \frac{2\gamma_{\text{surf}}}{d_2}\right)f_v. \tag{11}$$

Nanovoids could be considered as precipitates with zero stiffness. Unlike dense precipitates, dislocations shearing nanovoids do not generate APBs; thus, the strengthening arises solely from the creation of new matrix surfaces. For this case, with $\gamma_{\text{APB}} = 0$ J/m^2, the pair-coupling coefficient of 1/2 in Eqs. (4) and (5) should be replaced by 1 (Brown and Ham, 1971). The resulting CRSS expressions for strong-cutting and weak-cutting through voids become

$$\tau_{\text{strong}} = \frac{2\gamma_{\text{surf}}}{L} + \frac{2\gamma_{\text{surf}}f_v}{d_2} \tag{12}$$

and

$$\tau_{\text{weak}} = \frac{2\gamma_{\text{surf}}}{L}\sqrt{\frac{\gamma_{\text{surf}}b}{T^d}} + \frac{2\gamma_{\text{surf}}f_v}{d_2}, \tag{13}$$

respectively. Since both L and d_2 scale with the nanovoid diameter d_v, Eqs. (12) and (13) indicate that the strengthening effect increases inversely with d_v. Consequently, a pronounced rise in yield strength is expected as the nanovoid size decreases.

In general, a dislocation moves along the path of least slip resistance. Focusing on the physical mechanisms underlying nanovoid-regulated strengthening in porous gold, the increase in slip resistance can be attributed to the competition among the Orowan bypassing, strong-cutting, and weak-cutting mechanisms. Accordingly, the strengthening contribution τ_i^v in Eq. (7) due to nanovoids is proposed as

$$\begin{aligned}\tau_i^v &= \min\left\{\tau_{\text{Orowan}},\ \tau_{\text{strong}},\ \tau_{\text{weak}}\right\}\\ &= \min\left\{\frac{2T^d}{bL},\ \frac{2\gamma_{\text{surf}}}{L} + \frac{2\gamma_{\text{surf}}f_v}{d_2},\ \frac{2\gamma_{\text{surf}}}{L}\sqrt{\frac{\gamma_{\text{surf}}b}{T^d}} + \frac{2\gamma_{\text{surf}}f_v}{d_2}\right\}.\end{aligned} \tag{14}$$

The dislocation line tension T_d reported in the literature varies considerably. To minimize artificial influences in numerical simulations, T_d is uniformly set to $T_d = \mu b^2/4$, following Reppich (1975), which is notably smaller than $T_d = \mu b^2/2$ for the Orowan mechanism (Li et al., 2024).

In general, spherical voids elongate into ellipsoid under multiaxial stress loading. The aspect ratios and orientations of ellipsoidal voids could result in plastic anisotropy and damage anisotropy even for isotropic metallic materials (Nasir et al., 2025). However, as supported by our experimental results in Fig. A.1 of Appendix A and molecular dynamics simulations at relatively small strains (Chandra et al., 2017; Jing et al., 2018; Zhu et al., 2023; Lin et al., 2026), nanovoids are assumed to remain approximately spherical during deformation to simplify the modeling and analysis. As the void diameter d_v evolves due to void growth, the strengthening τ_i^v determined by Eq. (14) also varies during numerical simulations. The detailed derivation for the evolution of d_v is provided in Appendix A.

3. Mechanical behaviors and strengthening mechanism

3.1. Finite element model and validation of material parameters for dense gold

Section 3.1 focuses on the macroscopic mechanical response of dense gold to validate the intrinsic material parameters. For dense gold, voids with irregular shape may nucleate and grow during plastic deformation. Although these deformation-induced voids may play a role in impeding dislocation movement, in general they do not contribute to strengthening. The softening effect significantly surpasses the possible strengthening effect due to irregular voids and the associated localized stress concentration, accelerating material fracture, regardless of the nucleation and growth rate of voids. In contrast, nanovoids intentionally introduced prior to deformation (e.g., in porous gold) interact with dislocations from the onset of plastic flow, thereby increasing slip resistance and yield strength via Orowan or cutting mechanisms. Accordingly, in the simulations for dense gold, the strengthening contribution from voids is set to zero ($\tau_i^v \equiv 0$ MPa) in Eq. (7).

Fig. 1a illustrates the polycrystalline finite element model comprising 891 grains used in the numerical simulations. As demonstrated in

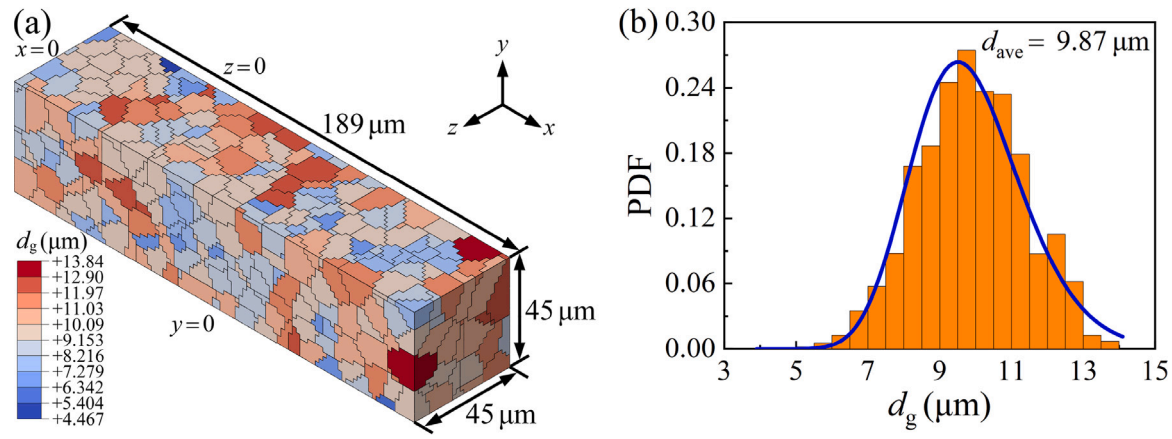

Fig. 1. Finite element model of polycrystalline gold: (a) Dimensions of sample containing 891 grains. (b) Volume-weighted probability density function (PDF) of grain diameter.

our previous work (Han et al., 2026), the element length of $L_e = 1.8$ μm could obtained convergent numerical results for porous metallic materials. The corresponding volume-weighted average grain diameter $d_{ave} = 9.87$ μm shown in Fig. 1b aligns with the experimentally measured average grain size of 10 μm (Chen et al., 2024). For dense gold, voids nucleate and grow as plastic strain increases. The evolution of the void volume fraction is described by the phenomenological law (Zhang et al., 2025)

$$\dot{f}_v = \frac{f_N}{s_N\sqrt{2\pi}} \exp\left[-\frac{1}{2}\left(\frac{\varepsilon_{mp}^{eq} - \varepsilon_N}{s_N}\right)^2\right] \dot{\varepsilon}_{mp}^{eq} + (1 - f_v)\mathrm{trace}(\mathbf{D}_p), \tag{15}$$

where f_N, s_N, and ε_N are dimensionless parameters characterizing the nucleation rate of new voids, and the microscopic equivalent plastic strain is defined as $\varepsilon_{mp}^{eq} = \int_0^t \sqrt{(2/3)\mathbf{D}_{mp} : \mathbf{D}_{mp}}dt$ with $\mathbf{D}_{mp} = \sum_{i=1}^{N_s} \dot{\gamma}_i[\mathbf{N}_i^{eff} + (\mathbf{N}_i^{eff})^T]/2$.

Table 1 summarizes the material parameters used for modeling dislocation slip and void evolution in dense polycrystalline gold. The shear modulus μ at ambient temperature $T = 300$ K is estimated by the Voigt–Reuss–Hill average (Hill, 1952). The parameters for temperature-dependent elastic constants $C_{ij}(T) = C_{ij}^0 - S_{ij}/[\exp(T_{ij}/T) - 1]$ ($i = 1, 4$ and $j = 1, 2, 4$) are listed in Table 2 (Olsson, 2015), where C_{ij}^0 is the elastic constant at $T = 0$ K, S_{ij} and T_{ij} are the corresponding fitting coefficients. The initial void volume fraction is taken as an extremely small value, $f_v^0 = 0.0001$, ensuring no influence on the initial yielding behavior. The critical annihilation distance between two opposite dislocations is fitted as $y_c = 34b$. In addition, the other parameters are also fitted through the experimentally measured nominal stress–strain curve. In all simulations, models with zero internal void pressure are symmetrically constrained at the surfaces of $x = 0$ μm, $y = 0$ μm, and $z = 0$ μm. Meanwhile, the surface at $x = 189$ μm is uniaxially stretched along the x-direction at a nominal strain rate of $\dot{\varepsilon}_{11}^{nom} = 0.002$/s, consistent with our experimental conditions (Chen et al., 2024).

Fig. 2 compares the nominal stress–strain (σ_{11}^{nom}–ε_{11}^{nom}) curves obtained from finite element simulations and experiments for polycrystalline dense gold under uniaxial tension. The simulated curve shows excellent agreement with the experimental result at $\varepsilon_{11}^{nom} < 0.15$, in which the localized necking is imperceptible. Following the conventional definition, the flow stress at 0.2% offset strain is referred to as yield strength. In addition, the strain corresponding to the maximum flow stress on σ_{11}^{nom}–ε_{11}^{nom} curve denotes uniform tensile strain, which marks the initiation of local necking in materials. The yield strength $\sigma_y^{dense} = 90.33$ MPa and uniform tensile strain $\varepsilon_u^{dense} = 0.108$ predicted by the simulation are consistent with the measured values $\sigma_y^{dense} = 85.27$ MPa and $\varepsilon_u^{dense} = 0.115$ in our experimental study (Chen et al., 2024), thereby confirming that the present model accurately

Table 1
Material parameters for dislocation slip and void evolution in dense single-crystal gold.

Parameters	Values	References
K	2.5	Fitted parameter
b	0.289 nm	Zhang et al. (2022)
f_v^0	0.0001	Fitted parameter
f_N	0.02	Chakraborty and Biner (2015)
m	0.05	Fitted parameter
q_1	1	Han et al. (2013)
q_2	1	Han et al. (2013)
s_N	0.02	Chakraborty and Biner (2015)
y_c	9.826 nm	Fitted parameter
α	0.32	Fitted parameter
$\dot{\gamma}^0$	0.0001/s	Xiao et al. (2015)
ε_N	0.08	Chakraborty and Biner (2015)
λ	1	Han et al. (2013)
μ	28.06 GPa	Voigt–Reuss–Hill average
ρ_i^0	1.06×10^{14}/m^2	Fitted parameter

Table 2
Temperature-dependent elastic constants for dense single-crystal gold (Olsson, 2015).

Elastic constants	C_{ij}^0 (GPa)	S_{ij} (GPa)	T_{ij} (K)
C_{11}	201.6	8.467	240.7
C_{12}	176.1	10.566	219.6
C_{44}	47.5	1.140	87.5

captures the macroscopic mechanical performances and validating both the constitutive formulation established in Section 2 and the material parameters summarized in Tables 1 and 2. In addition, the fundamental mechanism underlying marked discrepancies at large strains is revealed in Section 3.2.

3.2. Nanovoid-regulated mechanical performance of porous gold

For metallic materials with low yield strength, the growth of pre-existing voids is energetically more favorable than the nucleation of new ones (Ramesh, 2009). Given that $\sigma_y^{dense} = 85.27$ MPa of the dense gold in the experiment is relatively low, the growth rate of the void volume fraction is simplified as $\dot{f}_v = (1 - f_v)\mathrm{trace}(\mathbf{D}_p)$ in the following simulations for the porous gold samples in Table 3 (Chen et al., 2024).

As analyzed in Section 2.2, dislocations can cut through nanovoids, and the associated formation of new matrix surfaces might dominate the strengthening of the material. For FCC gold, dislocation slip primarily occurs on the {111}⟨110⟩ system at ambient temperature. Therefore, the increase in the CRSS of the porous gold arising from the cutting

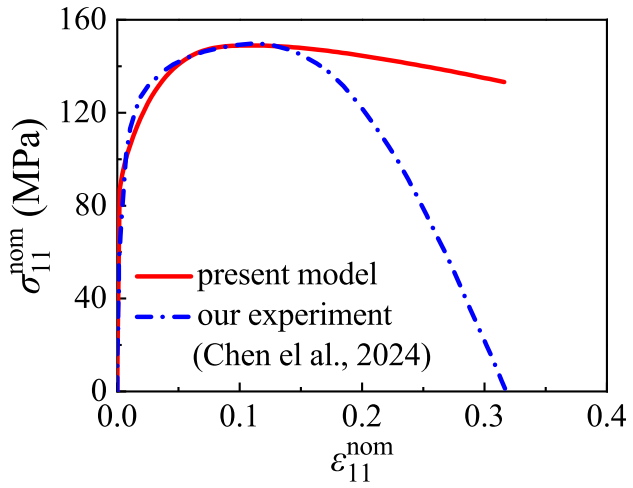

Fig. 2. Comparison of nominal stress–strain curves under uniaxial tension along the x-direction between numerical simulations and experimental results for polycrystalline dense gold.

Table 3
Initial diameters and volume fractions of nanovoids in samples (Chen et al., 2024).

Sample	1	2	3	4	5
d_v^0 (nm)	180	92	83	45	18
f_v^0	0.0691	0.0462	0.1170	0.0597	0.0615

mechanism is governed by the surface energy $\gamma_{surf} = 1.283$ J/m^2 of the close-packed {111} plane in Eq. (14) (Vitos et al., 1998). The line length of edge dislocations is estimated as $d_2 = d_v$. Moreover, nanovoids can promote dislocation nucleation and multiplication (Chen et al., 2024), thereby enhancing the material's overall strain-hardening capacity. To capture this effect, the propagation coefficient is adjusted to $K = 2.3$ for porous gold, slightly lower than $K = 2.5$ for dense gold. This is a rough qualitative modification for dimensionless parameter K, as it is difficult to microscopically measure the dynamic evolution rate of dislocation density in the experimental study for the porous gold with dispersed nanovoids. All other material parameters remain the same as those listed in Tables 1 and 2.

Fig. 3 shows the nominal stress–strain curves and yield strengths obtained from numerical simulations and experimental measurements for samples with various initial diameters and volume fractions of nanovoids, as listed in Table 3. The simulated results exhibit good agreement with experiments, except for a relatively large deviation observed in the sample with $d_v^0 = 18$ nm and $f_v^0 = 0.0615$. These results demonstrate that the proposed physics-based constitutive model in Section 2, which requires no empirical fitting parameters for τ_v, can precisely describe the strengthening effect induced by nanovoids, despite the underlying microscopic mechanisms not being fully elucidated.

Using the yield strengths and uniform tensile strains of the dense gold in Section 3.1 as benchmarks, Fig. 4 compares the experimental and numerical results for the normalized yield strengths $\bar{\sigma}_y$ and normalized uniform tensile strains $\bar{\varepsilon}_u$ of all samples, where $\bar{\sigma}_y = \sigma_y^{porous}/\sigma_y^{dense}$, $\bar{\varepsilon}_u = \varepsilon_u^{porous}/\varepsilon_u^{dense}$, and σ_y^{porous} and ε_u^{porous} denote the yield strength and uniform tensile strain of the porous gold with dispersed nanovoids, respectively. The numerical predictions agree well with the experimental data, successfully reproducing the remarkable strength–ductility trade-off observed in porous gold. The values of $\bar{\varepsilon}_u$ obtained from numerical simulations approach the lower bounds of the experimental results at relatively large nanovoids. The underlying microscopic mechanisms responsible for the nanovoid-induced strengthening and the simultaneous enhancement of strength and ductility at larger void sizes are discussed in detail below.

Using Eqs. (9), (12), and (13) in Section 2.2, Fig. 5 shows the initial increase in CRSS resulting from the Orowan, strong-cutting, and weak-cutting mechanisms at an initial void volume fraction of $f_v^0 = 0.05$. In contrast to the decreasing trend of the weak-cutting contribution in precipitate-strengthened alloys (Fang et al., 2019), the strengthening effect of the weak-cutting mechanism arising from dislocation–nanovoid interactions increases monotonically with decreasing void size. More importantly, the CRSS values associated with the weak-cutting mechanism remain lower than those predicted by the Orowan and strong-cutting mechanisms over the entire void-size range, with no intersection points indicating a mechanism transition. This result suggests that the weak-cutting mechanism — associated with the formation of new matrix surfaces — possesses the lowest critical resolved shear stress among all interaction modes. Hence, it is the easiest way to activate during plastic deformation and thus dominates the dislocation slip behavior in porous gold containing dispersed nanovoids.

To further identify the dominant role of the weak-cutting mechanism, Fig. 6 presents the evolution of τ_v with void growth at given f_v^0 and d_v^0, using Eqs. (9), (12), (13), (A.4) for all samples in Table 3. Both the initial and evolving values of τ_v from the weak-cutting mechanism remain substantially smaller than those from the Orowan and strong-cutting mechanisms throughout nanovoid growth. Meanwhile, the existing direct experimental observations and molecular dynamics simulations for different metallic materials, containing the high-entropy alloys as well as the irradiated copper, tungsten, and nickel with helium bubbles, indicate a cutting behavior in dislocation–nanovoid interaction (Ding et al., 2016a,b; Ji et al., 2023; Liu and Demkowicz, 2023; Lin et al., 2026), despite τ_{Orowan}, τ_{strong}, and τ_{weak} according to Eq. (14) mathematically showing different trends with the variation of μ and γ_{surf} and the possible transition in dominant strengthening mechanism. Therefore, incorporating the above theoretical results and observed cutting behaviors between dislocations and nanovoids in different metallic materials, the weak-cutting mechanism associated with the formation of new matrix surfaces is identified as the fundamental physical origin of the observed strengthening in porous metallic materials with dispersed nanovoids.

Both the experimental observations and finite element simulations in Fig. 4 reveal a synergistic enhancement of strength and ductility at relatively large void sizes. This strength–ductility synergy originates from two concurrent effects, the nanovoid-facilitated dislocation propagation and the nanovoid growth-induced increase in the strengthening contribution. As demonstrated previously, nanovoids in porous gold promote dislocation nucleation and multiplication (Chen et al., 2024), thereby elevating the dislocation storage capacity. Considering the saturated dislocation density $\rho_i^{sat} = 1/(2Ky_c)^2$ (Han et al., 2023), reducing the parameter K from 2.5 to 2.3 yields an increase in the saturated dislocation strengthening $\tau_i^d = \alpha\mu b\sqrt{\rho_i^{sat}}$ from 52.8 to 57.4 MPa. This enhanced ability to propagate dislocations contributes to greater macroscopic strain hardening, delays the onset of necking, and improves material ductility.

More importantly, Fig. 6 demonstrates that the strengthening effect associated with the weak-cutting mechanism increases substantially during void growth across all samples. Taking the sample with $d_v^0 = 92$ nm and $f_v^0 = 0.0462$ as an example, the value of τ_v described by the weak-cutting mechanism rises significantly from 10.65 to 24 MPa, as f_v increases from 0.0462 to 0.2. This pronounced rise in τ_v can counteract, or even exceed, the void-induced softening during nanovoid growth, thereby serving as another critical factor suppressing localized necking. Consequently, the combination of nanovoid growth-induced strengthening under the weak-cutting mechanism and nanovoid-enhanced dislocation accumulation gives rise to the observed improvement in ductility of porous metallic materials with dispersed nanovoids, delaying material fracture.

In addition, Fig. 3a–e indicates significant differences between the experimental and simulated nominal stress–strain (σ_{11}^{nom}–ε_{11}^{nom}) curves at fracture stage in the large strain regions, which can be attributed to the

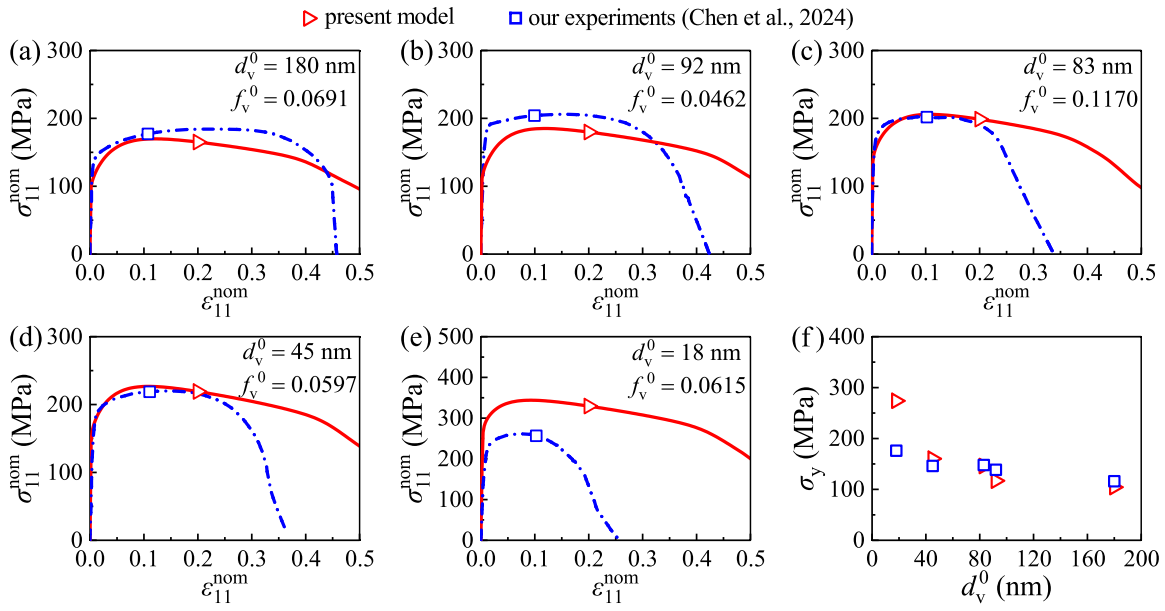

Fig. 3. Nominal stress–strain curves (a–e) and yield strengths (f) obtained from numerical simulations and experimental measurements for porous gold samples with different initial nanovoid diameters and volume fractions listed in Table 3.

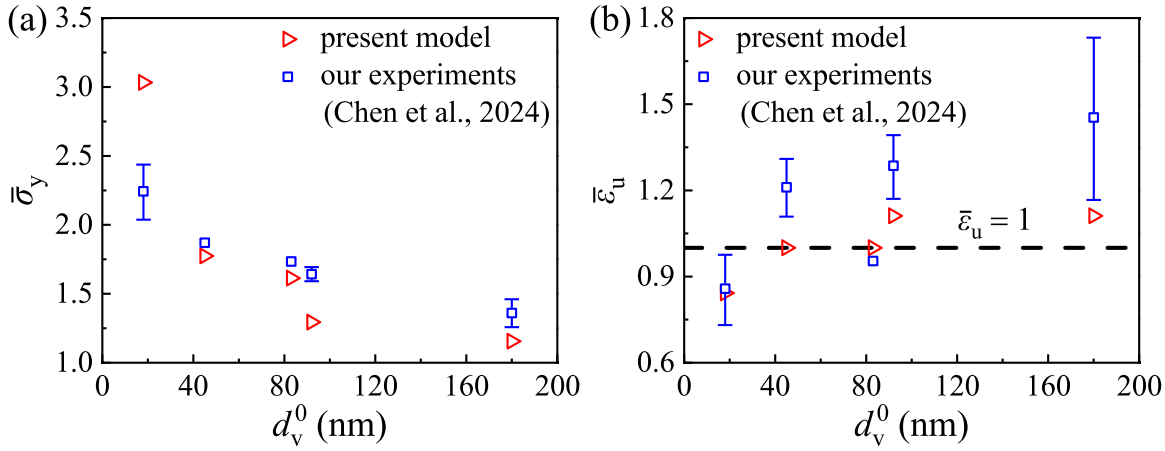

Fig. 4. Normalized yield strengths $\bar{\sigma}_y$ (a) and normalized uniform tensile strains $\bar{\varepsilon}_u$ (b) as functions of initial void diameter d_v^0, comparing numerical simulations with experimental results.

neglect of void coalescence in the present finite element simulations. With increasing plastic deformation, neighboring voids begin to coalesce, leading to a substantial rise in the effective void volume fraction and a rapid loss of load-carrying capacity (Tvergaard and Needleman, 1984; Meng et al., 2025; Patil et al., 2026). Meanwhile, coalescence in local regions transforms clusters of spherical nanovoids into irregular large voids, thereby eliminating the nanovoid strengthening effect. These two processes together account for the sharp stress drop of porous gold at large strains. The significant rise in the effective void volume fraction due to the coalescence mechanism is also applicable to interpret the discrepancy between the experimental and numerical results for dense gold at large strains observed in Fig. 2.

As shown in Fig. 3f, the experimentally measured yield strength is σ_y^{porous} = 176 MPa for the sample with d_v^0 = 18 nm and f_v^0 = 0.0615, around 35.7% less than the corresponding simulated value of σ_y^{porous} = 273.90 MPa. Previous simulations of uniaxial tension in isotropic plastic material have demonstrated the dependence of yield strength on the spatial distribution of voids (Bilger et al., 2005; Cruzado et al., 2024; Gao et al., 2026). At a certain void volume fraction, the samples containing the connected and disconnected void clusters exhibit lower yield strengths than those with uniformly distributed voids as well as the theoretical prediction of the Gurson model, as the nonuniformity increases the effective void volume fraction. For the sample with d_v^0 = 18 nm and f_v^0 = 0.0615, the void number density is nearly three orders of magnitude higher than that of the sample with d_v^0 = 180 nm and f_v^0 = 0.0691, resulting in a greater probability of void clustering, as confirmed by scanning electron microscopy in Fig. 7. Since the current constitutive model neglects the additional softening induced by such nonuniform void distributions, the simulated yield strength is markedly higher than the experimental value for the sample of d_v^0 = 18 nm with f_v^0 = 0.0615. Developing a homogenized framework that quantitatively captures the effect of nonuniform void distribution on yield strength will be a valuable direction for future work. In addition, Fig. 7 also indicates a nonuniform size distribution feature of nanovoids. To more accurately quantify the strengthening effect, the void size distribution-weighted sum for the slip resistance is a promising strategy (Fang et al., 2019).

Fig. 8 shows the evolution of reciprocal $1/\Phi$ of reduction in cross-sectional area with increasing nominal strain ε_{11}^{nom}, where $\Phi = 1 - S/S_0$ with S and S_0 denoting the current and initial cross-sectional areas at

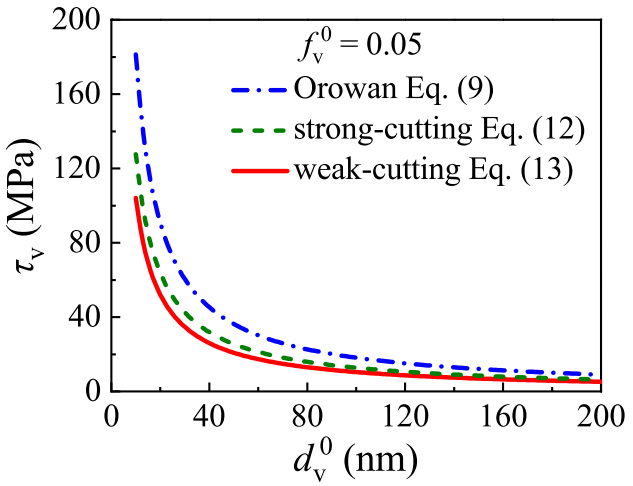

Fig. 5. Strengthening effects of different dislocation–void interaction mechanisms as functions of initial void diameter d_v^0 at initial void volume fraction $f_v^0 = 0.05$.

the initial position $x = 189$ μm in Fig. 1a, respectively. A more rapid decrease in $1/\Phi$ at a smaller d_v^0 suggests an accelerated development of localized necking, consistent with our previous theoretical analysis (Chen et al., 2024). Consequently, the ductility of porous gold decreases with decreasing d_v^0, as shown in Fig. 4b. The sample with $d_v^0 = 18$ nm and $f_v^0 = 0.0615$ exhibits lower ductility than the dense gold, owing to the most severe necking.

4. Theoretical models for optimizing strength–ductility balance

4.1. Theoretical prediction for yield strength

Previous numerical simulations have shown that the constitutive model proposed in Section 2 accurately captures the strengthening effect of nanovoids. However, the finite element simulations are computationally expensive. To improve efficiency, this subsection proposes a simplified theoretical model to estimate the yield strength of nanovoid-strengthened metallic materials.

At zero internal pressure ($P = 0$ MPa), recalling $q_1 = q_2 = \lambda = 1$, Eq. (1) reduces to

$$\Psi = \left(\frac{\tau_i}{\tau_i^{\mathrm{eff}}}\right)^2 + \frac{2}{45} f_v^{\mathrm{eff}} \left(\frac{\sigma_{\mathrm{eq}}}{\tau_i^{\mathrm{eff}}}\right)^2 + 2 f_v^{\mathrm{eff}} \cosh\left(\sqrt{\frac{3}{20}} \frac{\sigma_{\mathrm{m}}}{\tau_i^{\mathrm{eff}}}\right) - \left(f_v^{\mathrm{eff}}\right)^2 - 1 = 0. \tag{16}$$

In general, macroscopic yielding occurs when $\sigma_{\mathrm{eq}} = \sigma_{\mathrm{y}}^{\mathrm{porous}}$. At the microscopic scale, dislocation slip initiates when $\tau_i^{\mathrm{eff}} = \tau_i^{\mathrm{d}} + \tau_i^{\mathrm{v}}$, where the dislocation strengthening τ_i^{d} is calculated by $\tau_i^{\mathrm{d}} = \alpha\mu b\sqrt{\rho_i^0}$, and the void strengthening τ_i^{v} is determined by Eq. (13).

For uniaxial tension, the macroscopic hydrostatic stress is approximately $\sigma_{\mathrm{m}} = \sigma_{\mathrm{eq}}/3$ for polycrystalline samples at a small strain. Moreover, the average Schmid factor for an untextured FCC metal is $m_{\mathrm{Sch}} = 0.33$ (Carlton and Ferreira, 2007), leading to $\tau_i = m_{\mathrm{Sch}}\sigma_{\mathrm{eq}} = 0.33\sigma_{\mathrm{eq}}$ under uniaxial loading. Consequently, the yield strength of dense gold can be estimated as $\sigma_{\mathrm{y}}^{\mathrm{dense}} = \alpha\mu b\sqrt{\rho_i^0}/m_{\mathrm{Sch}} = 80.95$ MPa, agreeing well with $\sigma_{\mathrm{y}}^{\mathrm{dense}} = 85.27$ MPa in experiments and $\sigma_{\mathrm{y}}^{\mathrm{dense}} = 90.33$ MPa from the numerical simulations. With knowledge of $\sigma_{\mathrm{eq}} = \sigma_{\mathrm{y}}^{\mathrm{porous}}$, $\tau_i^{\mathrm{eff}} = \tau_i^{\mathrm{d}} + \tau_i^{\mathrm{v}}$, $\tau_i^{\mathrm{d}} = \alpha\mu b\sqrt{\rho_i^0}$, $\tau_i^{\mathrm{v}} = \tau_{\mathrm{weak}}$, $\sigma_{\mathrm{m}} = \sigma_{\mathrm{eq}}/3$, and $\tau_i = m_{\mathrm{Sch}}\sigma_{\mathrm{eq}}$, Eq. (16) can be rewritten as

$$\Psi = \left(\frac{m_{\mathrm{Sch}}\sigma_{\mathrm{y}}^{\mathrm{porous}}}{\alpha\mu b\sqrt{\rho_i^0} + \tau_{\mathrm{weak}}}\right)^2 + \frac{2}{45} f_v^{\mathrm{eff}} \left(\frac{\sigma_{\mathrm{y}}^{\mathrm{porous}}}{\alpha\mu b\sqrt{\rho_i^0} + \tau_{\mathrm{weak}}}\right)^2 + 2 f_v^{\mathrm{eff}} \cosh\left(\sqrt{\frac{1}{60}} \frac{\sigma_{\mathrm{y}}^{\mathrm{porous}}}{\alpha\mu b\sqrt{\rho_i^0} + \tau_{\mathrm{weak}}}\right) - \left(f_v^{\mathrm{eff}}\right)^2 - 1 = 0, \tag{17}$$

enabling efficient theoretical prediction of the yield strength $\sigma_{\mathrm{y}}^{\mathrm{porous}}$ once the initial void diameter d_v^0 and volume fraction f_v^0 are specified.

Table 4 compares the yield strength σ_{y} of the porous gold obtained from the theoretical prediction Eq. (17), experimental results, and finite element simulations. The yield strengths predicted by Eq. (17) agree well with both the numerical and experimental results at large void sizes but exhibit a noticeable deviation for the sample with $d_v^0 = 18$ nm and $f_v^0 = 0.0615$, demonstrating an efficient and physically interpretable approach for quantifying the macroscopic yield strength of porous metallic materials containing dispersed nanovoids.

Table 4
Comparison of yield strengths obtained from the theoretical prediction Eq. (17), finite element simulations, and experimental results for all samples.

Sample	d_v^0 (nm)	f_v^0	$\sigma_{\mathrm{y}}^{\mathrm{porous}}$ (MPa)		
			Prediction	Simulation	Experiment
1	180	0.0691	94.57	104.34	115.95
2	92	0.0462	106.65	116.90	138.54
3	83	0.117	135.76	145.72	147.91
4	45	0.0597	149.25	160.21	145.98
5	18	0.0615	264.45	273.90	175.97

Taking $\sigma_{\mathrm{y}}^{\mathrm{dense}} = 80.95$ MPa from the theoretical estimation and $\sigma_{\mathrm{y}}^{\mathrm{dense}} = 85.27$ MPa from the experimental results (Chen et al., 2024) as the respective benchmarks, we present in Fig. 9 the increment $\Delta\sigma_{\mathrm{y}} = \sigma_{\mathrm{y}}^{\mathrm{porous}} - \sigma_{\mathrm{y}}^{\mathrm{dense}}$ in yield strengths as functions of the initial void volume fraction f_v^0 at different values of the initial void diameter d_v^0. The comparisons show that the discrepancies are relatively small at large nanovoid sizes for the present theoretical model Eq. (17) and the fitted model in our previous work (Chen et al., 2024). As the present work neglects the additional softening due to nonuniform void distributions discussed in Section 3.2, $\Delta\sigma_{\mathrm{y}}$ monotonically increases with increasing f_v^0 at $d_v^0 = 20$ nm, differing from the decreasing trend of the fitted model at large f_v^0.

4.2. Quantitative criterion linking critical initial void diameter and volume fraction for strength–ductility synergy

The preceding results demonstrate that smaller nanovoids more effectively enhance yield strength but can severely degrade ductility when their size becomes extremely small. To overcome this strength–ductility trade-off, it is suggested that the average void diameter should exceed 10 nm (Chen et al., 2024). This subsection establishes a quantitative criterion that captures the coupled dependence between the critical initial void diameter and volume fraction required to achieve strength–ductility synergy.

Fig. 10 presents the contour maps of the nominal yield strength $\bar{\sigma}_{\mathrm{y}}$ and the nominal uniform tensile strain $\bar{\varepsilon}_{\mathrm{u}}$ as functions of the initial void diameter d_v^0 and volume fraction f_v^0 based on the finite element simulations. As d_v^0 decreases or f_v^0 increases, $\bar{\sigma}_{\mathrm{y}}$ increases monotonically, in contrast to the decreasing trend of $\bar{\varepsilon}_{\mathrm{u}}$. The contour line of $\bar{\varepsilon}_{\mathrm{u}} = 1$ in Fig. 10b indicates that the critical initial volume fraction of voids to maintain ductility depends on void size. In other words, the critical initial void diameter, above which ductility is not compromised, varies

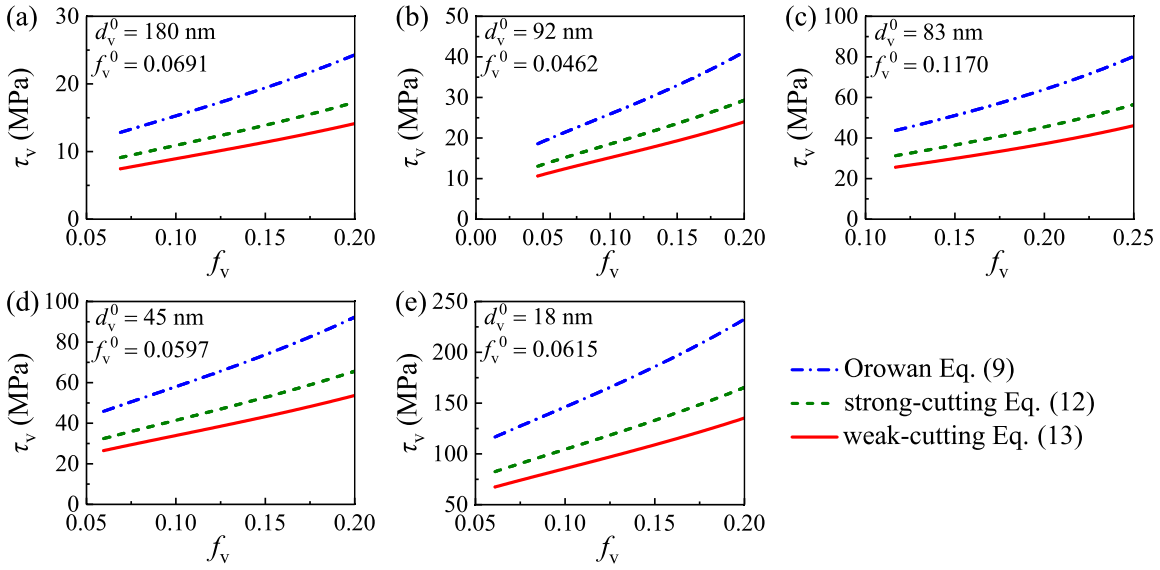

Fig. 6. Evolution of τ_v for different dislocation–void interaction mechanisms with nanovoid growth, calculated for all samples listed in Table 3.

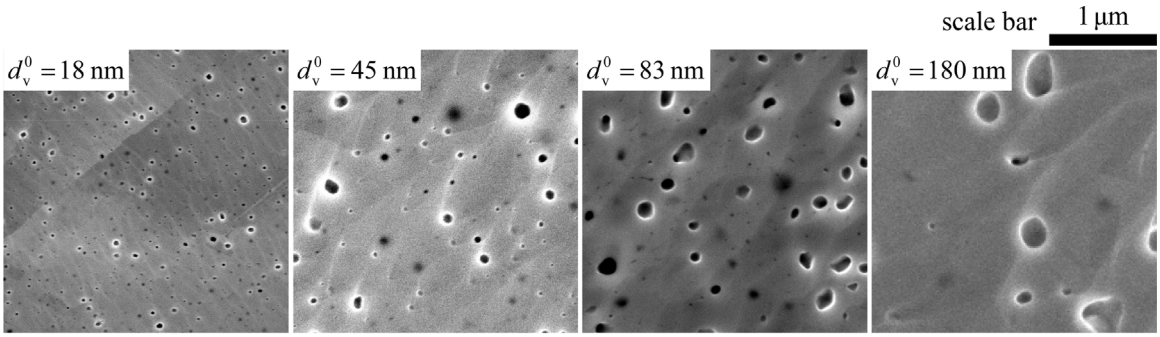

Fig. 7. Images of scanning electron microscopy for samples with different initial void diameters.

with f_v^0, deviating from the constant threshold of 10 nm previously suggested (Chen et al., 2024).

To conveniently determine this relationship, the following quantitative criterion is proposed

$$f_v^0 = 0.0004 d_v^0 / b. \tag{18}$$

Using Eq. (18), the critical initial volume fraction of voids for the sample with d_v^0 = 83 nm is f_v^0 = 0.1149 to retain $\bar{\varepsilon}_u$ = 1. Meanwhile, the sample with d_v^0 = 83 nm and f_v^0 = 0.1170 has the nominal uniform tensile strains of $\bar{\varepsilon}_u$ = 0.954 and 1 in the experiments and finite element simulations, respectively (Fig. 4b). Although the assumption of uniform void size adopted in the above numerical simulations deviates from the nonuniform distribution feature observed in Fig. 7, the good agreement between the extrapolated prediction from Eq. (18) and both experimental and numerical results validates the proposed criterion. Therefore, the present quantitative criterion in predicting ductility shows limited sensitivity to void size distribution. In addition, the corresponding evolutions of τ_v for all samples further identify that the weak-cutting mechanism dominates material strengthening, regardless of initial void sizes and volume fractions, as shown in Fig. B.1 in Appendix B.

In summary, Eqs. (17) and (18) together provide a practical framework to quantify both the yield strength and the critical combination of initial void diameter and volume fraction necessary to achieve strength–ductility synergy in porous metallic materials containing dispersed nanovoids.

5. Conclusion

This work has developed a physics-based crystal plasticity constitutive model that couples the competing dislocation–nanovoid interaction mechanisms to uncover the fundamental strengthening behavior of porous metallic materials containing dispersed nanovoids. The proposed theoretical yield strength model and the quantitative criterion for maintaining ductility show excellent agreement with both experimental observations and finite element simulations. This study advances the mechanistic understanding of nanovoid-regulated strengthening and provides theoretical guidance for the design of metallic materials with optimized strength and ductility. Key findings are summarized as follows.

(1) The weak-cutting mechanism, which involves the formation of new matrix surfaces during dislocation–nanovoid interactions, governs the strengthening of porous metallic materials across a wide range of void sizes, in contrast to the conventional Orowan mechanism.

(2) The strengthening contribution from the weak-cutting mechanism increases with void growth during plastic deformation. This trend, together with nanovoid-enhanced dislocation multiplication, improves

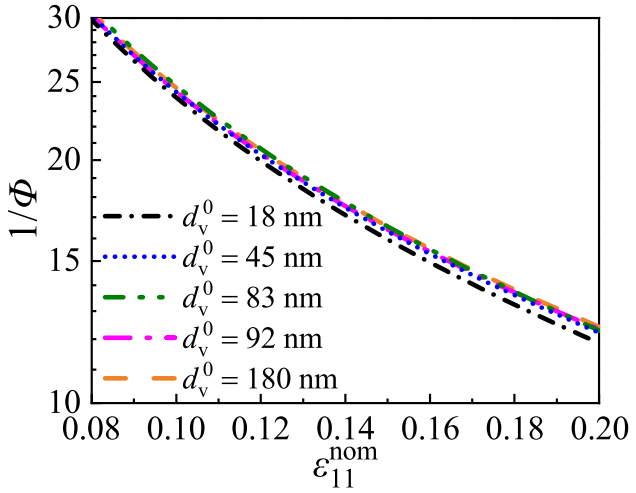

Fig. 8. Reciprocal $1/\Phi$ of reduction in cross-sectional area versus nominal strain ε_{11}^{nom} for different samples.

strain hardening, and delays the onset of localized necking, thereby enhancing ductility and delaying fracture at larger void sizes.

(3) At a fixed initial void volume fraction, reducing the void diameter intensifies localized necking, leading to a loss of ductility at extremely small void sizes. The critical void diameter below which ductility is compromised depends on the initial void volume fraction, and vice versa.

(4) To design porous metallic materials overcoming the strength–ductility trade-off, the yield strength can be quantified using the proposed theoretical prediction model Eq. (17), while the critical initial void diameter or volume fraction ensuring ductility can be determined using the quantitative criterion Eq. (18).

Even though the present work has successfully elucidated the strengthening effect of nanovoids, establishing a quantitative model for the softening effect due to the spatial cluster of nanovoids remains a meaningful challenge in future work.

CRediT authorship contribution statement

Quanfeng Han: Writing – review & editing, Writing – original draft, Software, Methodology, Investigation, Funding acquisition, Formal analysis, Conceptualization. **Jiaji Chen:** Writing – review & editing, Software, Methodology, Investigation, Formal analysis, Conceptualization. **Yufei Gao:** Investigation, Formal analysis. **Wenlong Li:** Investigation, Formal analysis. **Huiru Guo:** Investigation, Formal analysis. **Hui Wang:** Investigation, Formal analysis. **Yizhe Chen:** Writing – review & editing, Supervision, Methodology, Investigation, Funding acquisition, Formal analysis, Conceptualization. **Xin Yi:** Writing – review & editing, Supervision, Methodology, Investigation, Funding acquisition, Formal analysis, Conceptualization. **Lin Hua:** Writing – review & editing, Supervision, Investigation, Formal analysis.

Declaration of competing interest

The authors declare that they have no known competing financial interests or personal relationships that could have appeared to influence the work reported in this paper.

Acknowledgments

This work was supported by the National Natural Science Foundation of China (grant nos. 12402129, 12588201, and 52422510) and Natural Science Foundation of Hubei Province (grant no. 2025AFD124). Computational resources provided by the High-Performance Computing Platforms of Wuhan University of Technology and Peking University are acknowledged.

Appendix A. Derivation for evolution of void diameter

In Section 2.2, nanovoids are approximately spherical in the numerical simulations, consistent with our experimental results in Fig. A.1 and molecular dynamics simulations (Chandra et al., 2017; Jing et al., 2018; Zhu et al., 2023; Lin et al., 2026). This appendix details the derivation for the evolution of void diameter in the porous metallic materials.

For a certain integration point in the computational domain before deformation, the following relation holds among its associated volume V_{ipt}, void diameter d_v, void volume fraction f_v, and void number N_v

$$\frac{\pi(d_v^0)^3}{6} N_v = V_{ipt}^0 f_v^0, \tag{A.1}$$

where the superscript 0 denotes the initial state. Assuming that the void number N_v remains constant during deformation, one obtains at the end of the jth time increment

$$\frac{\pi(d_v^j)^3}{6} N_v = V_{ipt}^j f_v^j. \tag{A.2}$$

Combining Eqs. (A.1) and (A.2) gives the expression for the current void diameter as

$$d_v^j = d_v^0 \left(\frac{V_{ipt}^j f_v^j}{V_{ipt}^0 f_v^0} \right)^{1/3}. \tag{A.3}$$

Eq. (A.3) is employed in the simulations to update the void diameter.

Because the metallic matrix is nearly incompressible, V_{ipt} at any time can be approximated as $V_{ipt} = V_m/(1 - f_v)$, where V_m is the dense matrix volume belonging to the integration point. Substituting $V_{ipt}^0 = V_m/(1 - f_v^0)$ and $V_{ipt}^j = V_m/(1 - f_v^j)$ into Eq. (A.3) yields

$$d_v^j = d_v^0 \left[\frac{(1 - f_v^0) f_v^j}{(1 - f_v^j) f_v^0} \right]^{1/3}. \tag{A.4}$$

Eqs. (A.4) and (12) are used to theoretically quantify the evolution of τ_v due to void growth.

Appendix B. The evolution of τ_v at different initial values of void sizes and volume fractions

Fig. B.1 shows the evolution of τ_v with void growth at the range of 20 nm $< d_v^0 <$ 200 nm and 0.05 $< f_v^0 <$ 0.1. One can see that both the initial and evolving values of τ_v determined by the weak-cutting mechanism are remarkably less than those of strong-cutting and Orowan mechanisms, further supporting the dominant role of the weak-cutting mechanism in strengthening materials concluded in Section 3.2.

Data availability

Data will be made available on request.

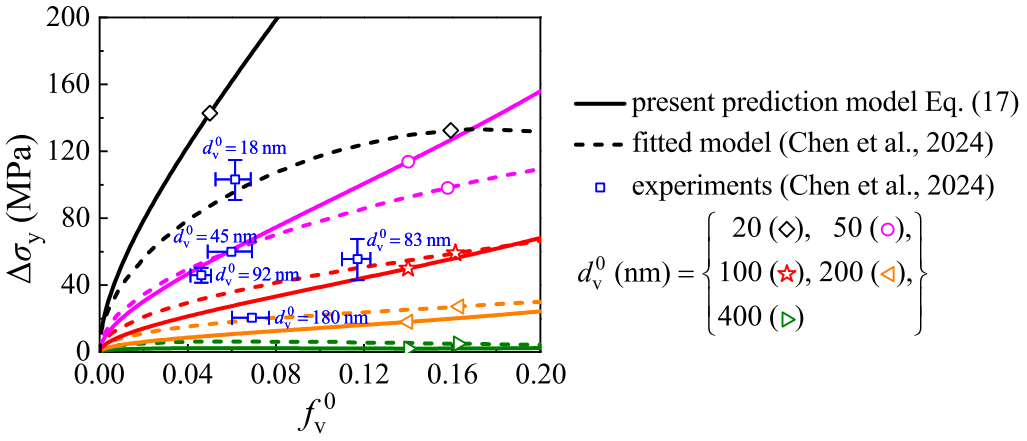

Fig. 9. Increment $\Delta\sigma_y$ in yield strength predicted by the present theoretical model Eq. (17) and by the fitted model of our previous work (Chen et al., 2024) as functions of initial void volume fraction f_v^0 at different initial void diameters d_v^0. The experimental results (Chen et al., 2024) are included for comparison.

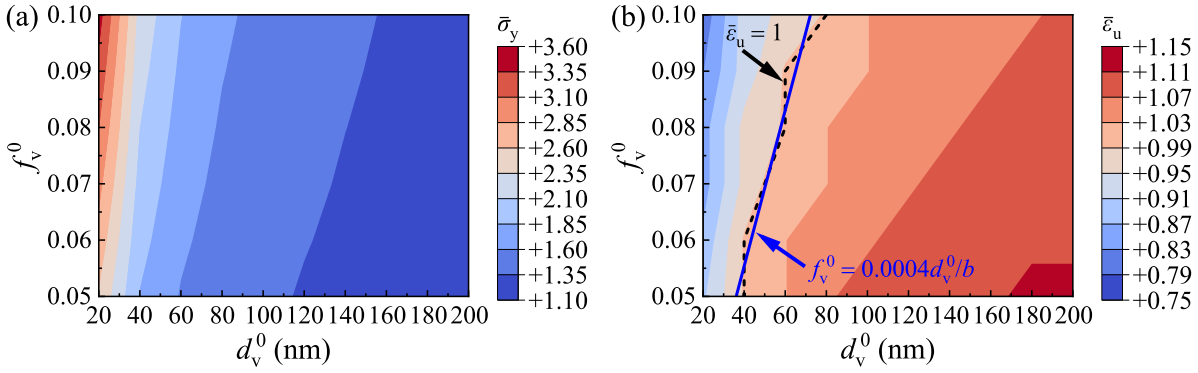

Fig. 10. Contour plots of nominal yield strength $\bar{\sigma}_y$ (a) and nominal uniform tensile strain $\bar{\varepsilon}_u$ (b) as functions of the initial void diameter d_v^0 and volume fraction f_v^0.

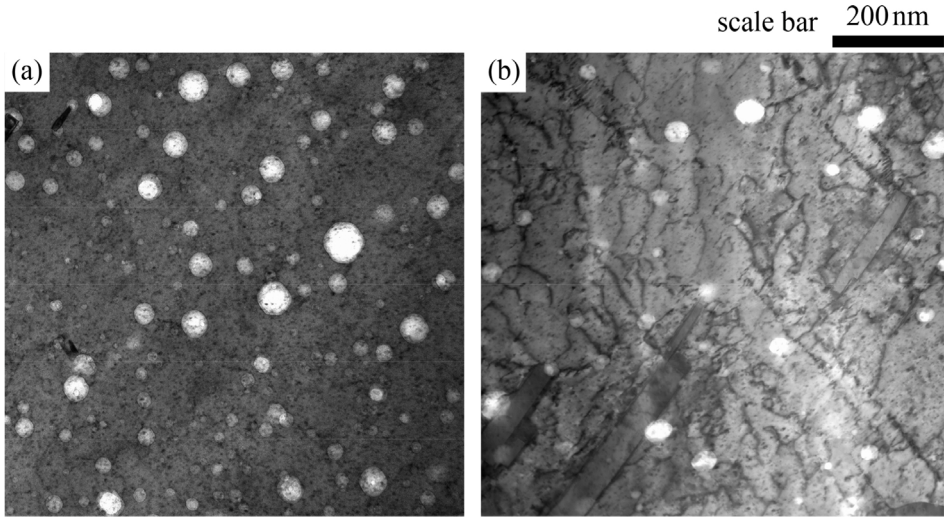

Fig. A.1. Images of transmission electron microscope for the sample with d_v^0 = 18 nm before (a) and after (b) uniaxial tensile loading.

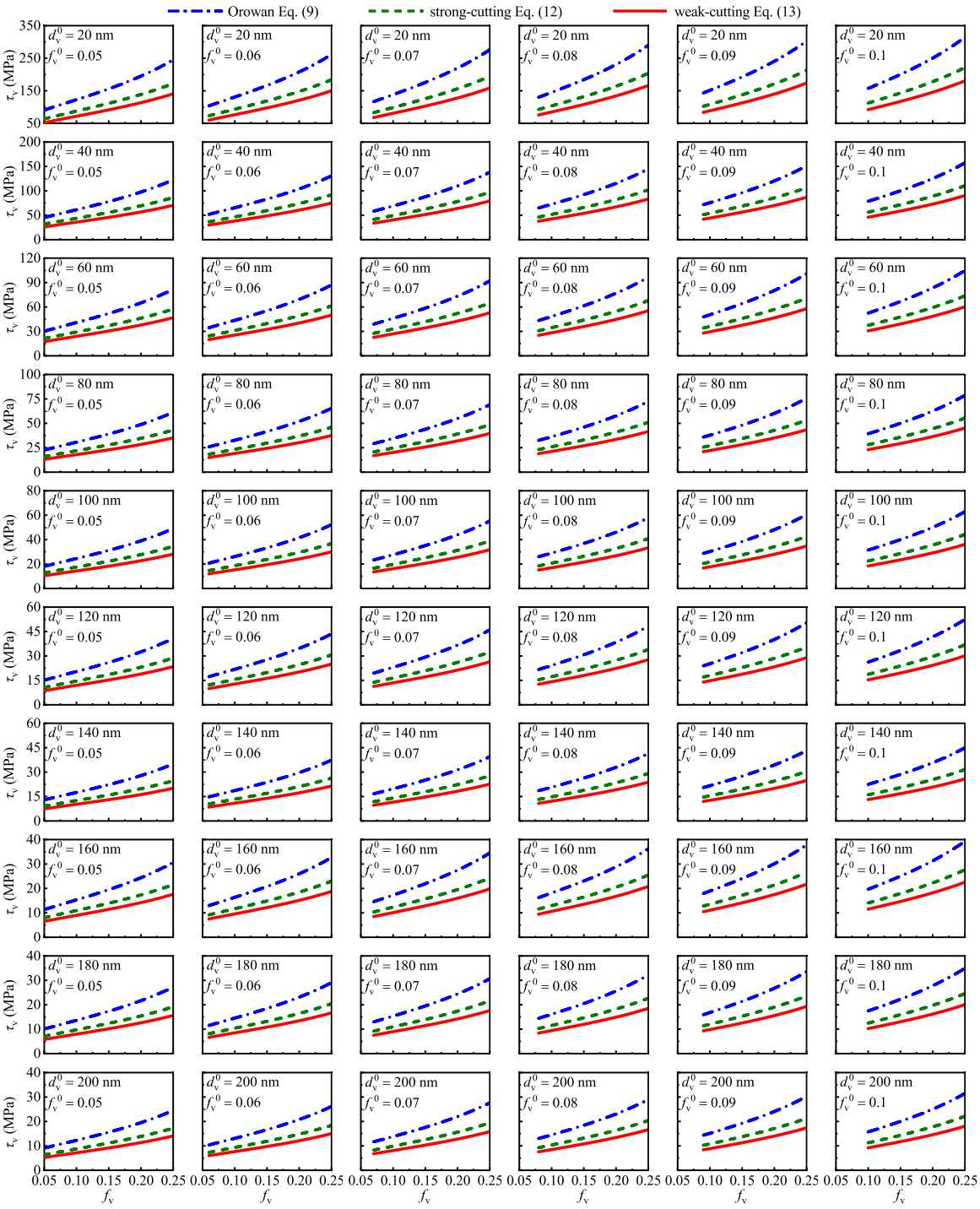

Fig. B.1. Evolution of τ_v for different dislocation–void interaction mechanisms with nanovoid growth, calculated for all samples in Fig. 10.

References

Bacon, D., Kocks, U., Scattergood, R., 1973. The effect of dislocation self-interaction on the Orowan stress. Phil. Mag. 28, 1241–1263.

Bilger, N., Auslender, F., Bornert, M., Michel, J.-C., Moulinec, H., Suquet, P., Zaoui, A., 2005. Effect of a nonuniform distribution of voids on the plastic response of voided materials: A computational and statistical analysis. Int. J. Solids Struct. 42, 517–538.

Brown, L., Ham, R., 1971. Dislocation-Particle Interactions. Elsevier, Barking, Essex, England..

Carlton, C., Ferreira, P., 2007. What is behind the inverse Hall–Petch effect in nanocrystalline materials? Acta Mater. 55, 3749–3756.

Chakraborty, P., Biner, S., 2015. Parametric study of irradiation effects on the ductile damage and flow stress behavior in ferritic-martensitic steels. J. Nucl. Mater. 465, 89–96.

Chandra, S., Samal, M., Chavan, V., Raghunathan, S., 2017. Void growth in single crystal Copper-an atomistic modeling and statistical analysis study. Phil. Mag. 98, 577–604.

Changizian, P., Yao, Z., Xu, S., Daymond, M., Griffiths, M., 2023. Mechanical behavior of recrystallized and precipitation-hardened Inconel X-750 before and after helium-implantation and proton irradiation. Mater. Charact. 202, 112970.

Chen, Z., Li, W., Ola, O., Feng, L., Zhang, X., Zhang, Y.-W., Yao, X., 2025. Hierarchical nanoporous-based design strategy towards ductileceramics with excellent strain hardening capability. Int. J. Plast. 194, 104487.

Chen, Y., Ma, X., Han, Q., Yang, D., Xiao, Y., Wang, H., Hua, L., 2026. Crystallographic texture and grain refinement regulated low-cycle fatigue performance of 6061-T6 aluminum alloy. Eng. Fail. Anal. 186, 110486.

Chen, J.-J., Xie, H., Liu, L.-Z., Guan, H., You, Z., Zou, L., Jin, H.-J., 2024. Strengthening gold with dispersed nanovoids. Science 385, 629–633.

Cruzado, A., Nelms, M., Benzerga, A., 2024. Effect of non-uniform void distributions on the yielding of metals. Comput. Methods Appl. Mech. Engrg. 421, 116810.

Dai, L., Fan, H., Wang, Y., Han, Q., Wang, H., Yang, D., Hua, L., Chen, Y., 2026. Bio-inspired interface-structure synergy unlocking synchronized helicoidal toughening in stiffness-mismatched hybrid materials. Adv. Compos. Hybrid Ma. http://dx.doi.org/10.1007/s42114-026-01896-3.

Ding, M.-S., Du, J.-P., Wan, L., Ogata, S., Tian, L., Ma, E., Han, W.-Z., Li, J., Shan, Z.-W., 2016a. Radiation-induced helium nanobubbles enhance ductility in submicron-sized single-crystalline copper. Nano Lett. 16, 4118–4124.

Ding, M.-S., Tian, L., Han, W.-Z., Li, J., Ma, E., Shan, Z.-W., 2016b. Nanobubble fragmentation and bubble-free-channel shear localization in helium-irradiated submicron-sized copper. Phys. Rev. Lett. 117, 215501.

Fang, Q., Li, L., Li, J., Wu, H., Huang, Z., Liu, B., Liu, Y., Liaw, P., 2019. A statistical theory of probability-dependent precipitation strengthening in metals and alloys. J. Mech. Phys. Solids 122, 177–189.

Gao, B., Huang, W., Wang, S., Liu, Z., Chen, X., Su, S., 2026. Investigation of void distribution effects on ductile failure via unit-cell calculations. Eur. J. Mech./A Solids 116, 105933.

Han, X., Besson, J., Forest, S., Tanguy, B., Bugat, S., 2013. A yield function for single crystals containing voids. Int. J. Solids Struct. 50, 2115–2131.

Han, Q., Li, J., Wang, H., Chen, Y., Yi, X., Hua, L., 2026. A physics-based crystal plasticity model for metallic material with highly pressurized bubbles. Eur. J. Mech./A Solids 118, 106101.

Han, Q., Li, J., Yi, X., 2023. Overcoming strength–ductility trade-off of nanocrystalline metals by engineering grain boundary, texture, and gradient microstructure. J. Mech. Phys. Solids 173, 105200.

Hill, R., 1952. The elastic behaviour of a crystalline aggregate. Proc. Phys. Soc. A 65, 349–354.

Hu, X., Koyanagi, T., Fukuda, M., Kumar, N., Snead, L., Wirth, B., Katoh, Y., 2016. Irradiation hardening of pure tungsten exposed to neutron irradiation. J. Nucl. Mater. 480, 235–243.

Huang, L., Wan, H., Han, Q., Wang, J., Yi, X., 2025. Mitigating surface notches for enhanced fatigue performance of metallic gyroid structures via contour scanning. Int. J. Mech. Sci. 286, 109913.

Hure, J., Courcelle, A., Turque, I., 2022. A micromechanical analysis of swelling-induced embrittlement in neutron-irradiated austenitic stainless steels. J. Nucl. Mater. 565, 153732.

Hutchinson, J., 1976. Bounds and self-consistent estimates for creep of polycrystalline materials. Proc. R. Soc. A 348, 101–127.

Ji, C., Hu, J., Zhuang, Z., Cui, Y., 2023. Atomistically-informed hardening and kinetics models of helium bubble in irradiated tungsten. Int. J. Plast. 165, 103620.

Jing, P., Yuan, L., Shivpuri, R., Xu, C., Zhang, Y., Shan, D., Guo, B., 2018. Evolution of spherical nanovoids within copper polycrystals during plastic straining: Atomistic investigation. Int. J. Plast. 100, 122–141.

Kim, Y., Cheng, Z., Gu, G., Lu, L., Kim, H., 2025. Mechanical behavior of gradient nanotwinned Cu: A dislocation-based constitutive model incorporating gradient effects. Mater. Sci. Eng. A 925, 147805.

Li, J., Han, Q., Han, X., Yi, X., 2024. Strength–ductility synergy in Mg–Gd–Y–Zr alloys via texture engineering in bi-directional forging. J. Magnes. Alloy. 12, 4709–4721.

Li, X., Jin, M., Zhang, Q., Wang, Y., Ma, X., Zhao, S., Chen, L., Cai, X., 2025. Multiple-mechanism and microstructure-based crystal plasticitysimulation of cyclic deformation in TRIP-assisted duplexstainless steels. Int. J. Plast. 195, 104521.

Lin, P., Li, Y., Cheng, Z., Lu, Y., 2026. Mechanistic insights into dislocation-void interactions in high-entropy alloys via molecular dynamics simulations. J. Mater. Sci. Technol. 269, 68–77.

Liu, T., Demkowicz, M., 2023. Effect of free surfaces on localized plastic deformation in single-crystal nickel containing helium bubbles and radiation-induced self-interstitial atom clusters. J. Nucl. Mater. 587, 154741.

Meng, Y., Song, W., Liu, S., Wang, Y., Li, W., Xiao, L., 2025. Grain size effect and structural heterogeneity in the shock-induced plastic deformation mechanism of nanocrystalline high-entropy alloys. Eur. J. Mech./A Solids 112, 105662.

Nasir, M.W., Muzammil, S., Chalal, H., Abed-Meraim, F., 2025. Void shape and orientation effects on anisotropic porousmaterial formability. Int. J. Mech. Sci. 307, 110902.

Olsson, P., 2015. First principles investigation of the finite temperature dependence of the elastic constants of zirconium, magnesium and gold. Comput. Mater. Sci. 99, 361–372.

Orowan, E., 1948. Symposium on internal stresses in metals and alloys. Inst. Met. Lond. 451–453.

Osetsky, Y., Bacon, D., Mohles, V., 2003. Atomic modelling of strengthening mechanisms due to voids and copper precipitates in α-iron. Phil. Mag. 83, 3623–3641.

Patil, S.A., Prüger, S., Roth, S., Kiefer, B., 2026. A finite element framework coupling chemo-mechanics and the non-local Gurson–Tvergaard–Needleman model for hydrogen-induced ductility loss in steels. Eur. J. Mech./A Solids 118, 106121.

Pham, M.-S., Liu, C., Todd, I., Lertthanasarn, J., 2019. Damage-tolerant architected materials inspired by crystal microstructure. Nature 565, 305–311.

Ramesh, K., 2009. Nanomaterials: Mechanics and Mechanisms. Springer, New York, United States of America.

Reppich, B., 1975. Strengthening mechanisms in MgO containing coherent stress-free precipitation particles–I. Theory. Acta Metall. 23, 1055–1060.

Roger, C., 2006. The Superalloys: Fundamentals and Applications. Cambridge University Press, New York, United States of America.

Tvergaard, V., Needleman, A., 1984. Analysis of the cup-cone fracture in a round tensile bar. Acta Metall. 32, 157–169.

Vitos, L., Ruban, A., Skriver, H., Kollár, J., 1998. The surface energy of metals. Surf. Energy 411, 186–202.

Xiao, X., Song, D., Chu, H., Xue, J., Duan, H., 2015. Mechanical properties for irradiated face-centred cubic nanocrystalline metals. Proc. R. Soc. A 471, 20140832.

Xie, H., Shao, J.-C., Zou, L., Jin, H.-J., 2023. Weak boundary enabled tensile ductility in dealloyed porous Fe alloy. Acta Mater. 243, 118501.

Yu, L., Sui, H., Liu, W., Chen, L., Liu, Y., Duan, H., 2020. A yield criterion for porous crystalline materials with inner pressure. Int. J. Solids Struct. 202, 511–520.

Yuan, Z., Chen, C., Zhang, X., Zhou, L., Wu, X., Yuan, F., 2025. Strain-rate and temperature dependent optimum precipitation sizes for strengthening in medium-entropy alloys. Int. J. Plast. 187, 104268.

Zhang, Y., Ding, K., Stangebye, S., Chen, D., Kacher, J., Pierron, O., Zhu, T., 2022. Atomistic modeling of surface and grain boundary dislocation nucleation in FCC metals. Acta Mater. 237, 118155.

Zhang, Z., Tang, Y., Zhao, Q., Huang, Q., Zhou, H., 2025. Theoretical modeling of phase boundary mediated extra tensile strength and plasticity in high entropy alloys. J. Mech. Phys. Solids 200, 106106.

Zhu, Q., Shao, J.-L., Wang, P., 2023. The dynamic response of He bubble in bicrystal copper under uniaxial compression and tension. J. Nucl. Mater. 574, 154200.